

Cite this: *Energy Environ. Sci.*, 2025, 18, 6577

# Failure mode diagnosis and stabilization of an efficient reverse-bias bipolar membrane CO<sub>2</sub> to CO electrolyzer†

Sven Brückner,<sup>‡a</sup> Oleksandr Bondarchuk,<sup>‡bcd</sup> Ana Araújo,<sup>be</sup> Wen Ju,<sup>id af</sup> Rosalía Cid,<sup>id g</sup> Elvira Paz,<sup>b</sup> Florian Krebs,<sup>a</sup> Olívia Salomé G. P. Soares,<sup>id e</sup> Isilda Amorim,<sup>b</sup> Zhipeng Yu,<sup>id b</sup> Pierre Schröer,<sup>a</sup> Philipp Hauke,<sup>a</sup> Manuel Fernando R. Pereira,<sup>id e</sup> Lifeng Liu<sup>id bh</sup> and Peter Strasser<sup>id \*a</sup>

Efficient and stable CO<sub>2</sub>-to-CO electrolyzers are key process components for the generation of green synthesis gas and its downstream conversion and valorization to carbonaceous e-chemicals and e-fuels. While alkaline CO<sub>2</sub> electrolyzers suffer from low CO<sub>2</sub> utilization due to cathodic carbonate formation and crossover, acidic CO<sub>2</sub> electrolyzers suffer from low CO faradaic efficiency. Reverse-bias bipolar membrane (BPM) cell architectures have been proposed to promote cathodic proton transport, yet resulted in limited cell lifetimes due to complex degradation and failure regimes. A thorough diagnosis of BPM cell dynamics is missing to date. Here, we build and diagnose an efficient zero-gap reverse-bias BPM CO<sub>2</sub>-to-CO electrolyzer cell deploying CO-selective single Ni atom cathode catalysts. We analyzed its key cell performance parameters and diagnosed the cell stability and failure regimes over 100 hours. The electrolyzer cell showed excellent performance up to 500 mA cm<sup>-2</sup> with CO faradaic efficiency near 100%. The proton-controlled ion transport in the cathode was directly confirmed by an experimental carbon cross-over coefficient (CCC) of zero, suggesting minimal carbon loss due to carbonate formation. This was coupled to a high single pass conversion of ~70% at the largest current densities and 60 vol% CO in the cell outlet, ideally suited for process cascade involving electro- or thermal catalytic steps. While use of a N<sub>2</sub> bleed for internal reference has been known to be critical for accurate evaluation of cell performance, we now propose the experimental N<sub>2</sub> vol% in the combined cell outlet and bleed flow to be also a valuable diagnostic tool to recognize and analyze cell failure regimes.

Received 1st April 2025,  
Accepted 21st May 2025

DOI: 10.1039/d5ee01817j

rsc.li/ees

## Broader context

Electrochemical CO<sub>2</sub> reduction is an emerging and promising technology for converting CO<sub>2</sub> into value-added products, thereby helping to close the anthropogenic carbon cycle. However, neutral-alkaline CO<sub>2</sub> electrolysis suffers from parasitic acid-base CO<sub>2</sub> consumption by hydroxide ions, leading to prohibitively low carbon utilization. Owing to their acidic cathode environments, bipolar membrane-based CO<sub>2</sub> electrolysis offers improved carbon efficiencies, yet brings along its own characteristic failure modes. Diagnostic tools that monitor, identify, and help mitigate failure modes are missing. This contribution reports experimental strategies to track and mitigate BPM cell failure to extend the lifetime of CO<sub>2</sub> electrolyzers.

<sup>a</sup> The Electrochemical Energy, Catalysis, and Materials Science Laboratory, Department of Chemistry, Chemical Engineering Division, Technical University Berlin, Berlin, Germany. E-mail: pstrasser@tu-berlin.de

<sup>b</sup> International Iberian Nanotechnology Laboratory (INL), 4715-330 Braga, Portugal

<sup>c</sup> SPIN-Lab Centre for Microscopic Research on Matter, University of Silesia in Katowice, 75 Pułku Piechoty Str. 1A, Chorzów 41-500, Poland

<sup>d</sup> Institute of Chemistry, University of Silesia in Katowice, 9 Szkolna Str., 40-006 Katowice, Poland

<sup>e</sup> LSRE-LCM – Laboratory of Separation and Reaction Engineering-Laboratory of Catalysis and Materials, Faculty of Engineering and ALiCE – Associate Laboratory in Chemical Engineering, Faculty of Engineering, University of Porto, 4200-465 Porto, Portugal

<sup>f</sup> Department of Electrochemistry and Catalysis, Leibniz Institute for Catalysis, 18059, Rostock, Germany

<sup>g</sup> Centre for Cooperative Research on Alternative Energies (CIC energiGUNE), Basque Research and Technology Alliance (BRTA), Alava Technology Park, Albert Einstein 48, 01510 Vitoria-Gasteiz, Spain

<sup>h</sup> Songshan Lake Materials Laboratory (SALB), Dongguan, Guangdong 523808, People's Republic of China

† Electronic supplementary information (ESI) available. See DOI: <https://doi.org/10.1039/d5ee01817j>

‡ The authors contributed equally.



## Introduction

Direct CO<sub>2</sub> electrolysis has emerged as a focal point of scientific exploration and technological advancements in the field of power-to-hydrocarbon e-fuels. Especially, the CO<sub>2</sub> to CO cascade has witnessed significant breakthroughs for its inherent high catalytic selectivity and process energy efficiency, and proper catalysts for this conversion can be broadly categorized into two classes: coin metals Ag and Au, where silver has garnered considerable attention,<sup>1–6</sup> and the more recent emergence of the family of metal–nitrogen–carbon (MNC) single site catalyst materials.<sup>7–12</sup>

Currently, our understanding indicates that both catalyst classes exhibit good selectivity and demonstrate the ability to achieve high current densities, while there is a considerable cost difference. However, there also remains a knowledge gap regarding the stability and degradation of these two classes of catalysts. On one hand, it is known that silver suffers from cathodic corrosion, akin to other noble metals such as gold and platinum.<sup>13,14</sup> On the other hand, despite their proven application in acidic proton exchange membrane environments, the stability of metal–nitrogen–carbon (MNC) catalysts against metal atom leaching is not fully understood. Computational calculations indicate that CO can stabilize lower coordinated Ni species,<sup>15</sup> which may also apply to NiNC catalysts. Moreover, MNC catalysts offer unique advantages in terms of relative intermediate binding energies to their coordinative single-metal active sites. This distinctive feature enhances the intrinsic selectivity of the single metal atom active sites toward CO<sub>2</sub> reduction compared to that toward hydrogen evolution, and it also allows for efficient metal utilization.<sup>16</sup> These characteristics create exciting opportunities for exploring and developing more efficient catalysts for sustainable CO<sub>2</sub> conversion at industrial scales.

To fully uncover the true potential of the catalyst, it is essential to evaluate its performance in a full two-electrode electrolyzer cell device. The zero-gap membrane electrode assembly (MEA) cell configuration provides closer proximity between the catalyst and the electrode, enabling efficient charge transfer and low potential losses. However, technical challenges such as flooding and salt precipitation must be addressed and overcome for optimal electrolyzer performance and stability. This work will address these issues.

In the zero-gap cell, salt precipitation caused by exceeding bicarbonate solubility limits has remained a key challenge that could be addressed by cathode water management or by choice of a suitable cation offering larger solubility limits.<sup>17</sup> The key advantage of a zero-gap cell is the significantly lower cell potential and energy efficiency compared to liquid cathode gap cells.<sup>6,12,18,19</sup> The choice of the type of ion transported across the solid electrolyte membrane offers options including the cation-exchange membrane (CEM), the anion-exchange membrane (AEM) and the bipolar membrane (BPM). BPM based electrolyzers have been operated in both reverse-bias and forward-bias modes. In forward-bias BPM electrolyzer designs, cathodic hydroxide anions are neutralized by acid-based

recombination inside the BPM minimizing CO<sub>2</sub> depletion by carbonate formation. The spontaneous recombination lowers required cell voltage. By contrast, the reverse bias mode generates a pH gradient by water dissociation. Protons channeled toward the cathode neutralize carbonate at the expense of cell voltage.

State-of-the-art efficient CO<sub>2</sub> electrolyzers have been designed using AEMs, thanks to the pH dependent Nernst potential of the competing proton discharge process. However, AEM based cells suffer from significant cathodic flow depletion: if every generated OH<sup>−</sup> is converted to CO<sub>3</sub><sup>2−</sup>, one loses around 7 ml A<sup>−1</sup> min<sup>−1</sup> CO<sub>2</sub>.<sup>20,21</sup> This drop in flow makes an accurate measurement of the cathodic gas outflow rate from the electrolysis cell critically important. Careless overestimation of cathode outlet flow rates can result in overestimated CO faradaic efficiencies and overestimated cell performance.<sup>11,12,22,23</sup> In addition to the gas flow depletion challenge in AEM cell designs, the use of non-noble Ni-based zero-gap anodes in direct contact with the AEM, even in presence of high-pH anolytes, is precluded by anodic corrosion due to low local pH caused by (bi)carbonate crossover.<sup>24,25</sup>

In this contribution, we design, operate, and diagnose an efficient reverse-bias, zero-gap BPM CO<sub>2</sub>-to-CO electrolyzer using an acid-stable NiNC single metal atom catalyst. The BPM dissociates water in the reverse bias mode and channels protons to the cathode, which recombine with catalytically generated OH<sup>−</sup>, thereby eliminating undesired cathodic (bi)carbonate accumulation and gas flow depletion.<sup>26–31</sup> At the same time, the acid-stable NiNC single metal atom catalyst with its low atomic H chemisorption<sup>32,33</sup> ensures high faradaic efficiencies toward CO. While we diagnose and identify the proton as the dominant transport ion at the cathode using the recently introduced kinetic carbon crossover coefficient (CCC),<sup>16</sup> we demonstrate, distinguish, and analyze common electrolyzer failure modes such as salt blocking at cell inlet and outlet. Our BPM electrolyzer could be continuously operated for over 100 h. It showed near 100% CO faradaic efficiencies at over 400 mA cm<sup>−2</sup> CO partial current density, coupled to 70% single pass conversion (SP) and a previously unachieved 60% CO-rich outlet gas stream associated with a low CO<sub>2</sub> stoichiometric ratio  $\lambda$ .

## CO<sub>2</sub> reduction catalyst synthesis and characterization

We synthesized a number of distinct NiNC catalysts (NiNC-600C, NiNC-800C, NiNC-1000C) from a Ni-imidazole framework precursor using a 2-step pyrolysis process at varying temperatures. The final pyrolysis step temperature is thereby eponymous. The catalysts obtained were characterized by scanning electron microscopy (SEM), transmission electron microscopy (TEM), N<sub>2</sub> adsorption/desorption isotherms, X-ray photoelectron spectroscopy (XPS), Fig. 1, elemental analysis, inductively-coupled plasma optical emission spectroscopy (ICP-OES, Table S2, ESI<sup>†</sup>) and X-ray diffractometry (XRD, Fig. S1, ESI<sup>†</sup>). SEM revealed (Fig. 1a, c and e) a slight morphology change with increasing



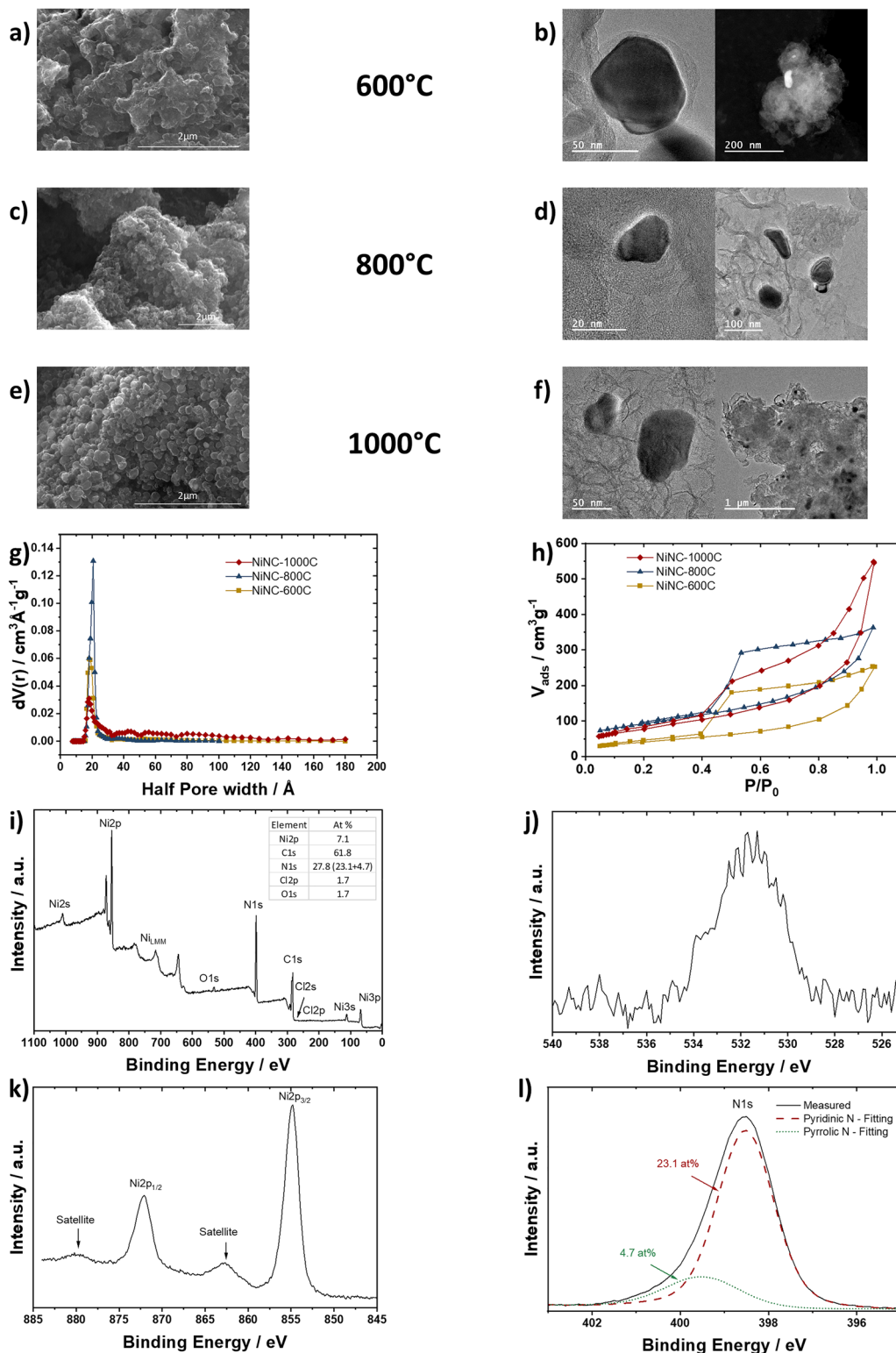


**Fig. 1** Characterization of the NiNC catalyst. (a) SEM and (b) TEM images of the NiNC-600C. (c) SEM and (d) TEM images of the NiNC-800C. (e) SEM and (f) TEM images of the NiNC-1000C. (g) Pore distribution and (h) adsorption/desorption isotherm plots. (i) survey XPS of NiNC-1000C, (j) insights of satellite and main peaks of nickel, (k) oxygen and (l) nitrogen, respectively.

pyrolysis temperature, with more flakes and particles rather than continuous carbon structures. At a smaller length scale, TEM images (Fig. 1b, d and f) suggested no significant differences from

earlier comparable synthesis results.<sup>16</sup> The morphology change is mirrored in the Brunauer–Emmett–Teller (BET) surface area values (Fig. 1g, h and Table S3, ESI<sup>†</sup>), where an increase in surface



area, mesopores, and micropores was observed from NiNC-600C to NiNC-800C. At even higher temperatures, the mesopores started to collapse coupled with lower BET values. During the pyrolysis, carbon-embedded metallic Ni nanoparticles formed, while the stacking order of the carbon increased with higher temperatures, seen by more prominent (002) carbon reflection in the XRD (Fig. S1, ESI†). Thanks to the final acid washing of all catalysts, accessible metallic Ni particles were removed to ensure no/low HER activity.

Fig. 1i presents the survey XPS spectrum of the NiNC-1000C sample. The strong C 1s signal is mainly due to the carbon framework, where the single atom nickel is embedded into. A small oxygen peak in Fig. 1j at  $\sim 532$  eV is due to typical surface contamination, like COOH, CO and COH. The shape and peak position of the O 1s signal apparently indicate no significant amount of metal oxides. The estimated atomic concentration Ni:N ratio is  $1:3.8 \approx 4$ , very different from that in the “Ni<sub>3</sub>N” (Note S1, ESI†). The Ni 2p<sub>3/2</sub> main peak position is at 854.9 eV (Fig. 1k), meaning the chemical shift of the Ni 2p level is larger by 1.3 eV than that of NiO (853.6 eV). The satellite peak is shifted by 7.9 eV to the higher binding energies from the main peak. The intensity of the satellite is 12% of the intensity of the main peak. This is a much smaller relative satellite intensity compared to the 77% for NiO. The Ni 2p<sub>3/2</sub> XPS peak of NiO is dominated by the 2p<sup>5</sup>d<sup>8</sup> core hole configuration<sup>34</sup> – the high spin configuration of Ni cation. According to Grosvenor *et al.* the relatively weak satellite, observed for NiNC-1000C, is indicative of low-spin configuration of Ni ions.<sup>35</sup> Given this and taking into account the substantial chemical shift of the main peak to higher binding energy together with the observed Ni:N concentration ratio, one could speculate that the dominating oxidation state of Ni in the NiNC-1000C sample is higher than +2 and the correspondent final state is 2p<sup>5</sup>d<sup>7</sup>. In the same time this conclusion is not in accord with the reported Ni 2p spectra for Ni(OH)<sub>2</sub>, where Ni is in +2 oxidation state, and Ni 2p<sub>3/2</sub> peak appears at 855.8 eV.<sup>36</sup> As an alternative explanation one can consider the square-planar structure where 4 nitrogen atoms are around Ni which is in low spin configuration and its oxidation state is +2 with the fully occupied 3d<sub>xy</sub>, 3d<sub>xz</sub>, 3d<sub>yz</sub>, 3d<sub>z<sup>2</sup></sub> orbitals and empty 3d<sub>x<sup>2</sup>-y<sup>2</sup></sub> orbital – similar to what can be found in nickel porphyrin.<sup>37</sup> To check this explanation out we performed XPS characterization of oxide free Ni porphyrin and Ni phthalocyanine films *in situ* grown *via* thermal evaporation. The results are presented in the ESI.†

The N 1s spectrum (Fig. 1l) exhibits a single peak with the maximum at 398.5 eV, shifted by 0.5 eV with respect to the “Ni<sub>3</sub>N” sample. The observed singlet shape of N 1s is in contrast to the nickel nitrides prepared in a similar way. Pyridinic and pyrrolic functional groups were reported based on the multiple component fitting of the N 1s spectra.<sup>10,38,39</sup> Fig. S7 (ESI†) compares N 1s spectra of the “Ni<sub>3</sub>N” with the N 1s spectrum from oxygen-free VN prepared *via* thermal nitridation of pure vanadium.<sup>40</sup> The “Ni<sub>3</sub>N” and VN spectra reveal quite similar asymmetric shapes, characteristic of conductive materials, while the NiNC-1000C spectrum has a clear minimum on the

higher binding energy side of the N 1s peak. The minimum is followed by the onset of the inelastic losses. The distance from the onset to the N 1s core-level peak can be used to determine the band gap ( $\sim 4.5$  eV) or, rather, the HOMO–LUMO gap according to Nichols *et al.*<sup>41</sup> and references therein. A further comparison between NiNC-100C and reference materials like Ni-TPP, Ni PC and Ni<sub>3</sub>N can be found in the Note S1 (ESI†).

## Design and performance of a zero-gap BPM electrode assembly

Mass transport and solubility limitations of gaseous CO<sub>2</sub> in liquid aqueous electrolytes preclude the use of fully immersed electrodes, where industrial current densities on the order of several hundreds of mA cm<sup>-2</sup> are of the essence. Instead, gas diffusion electrodes (GDEs) composed of a porous transport layer (PTL) equipped with a catalyst-coated micro porous layer (MPL) separate the CO<sub>2</sub> gas channel from the liquid catholyte compartment (one-gap design) or from the ion exchange membrane (zero-gap design). Fig. 2 displays the zero-gap CO<sub>2</sub> electrolyzer cell design where the anodic and cathodic flow fields are integrated into the current collectors. In between the two current collectors is the BPM assembly consisting of the anode, the BPM and the NiNC-catalyst on the carbon cloth PTL (see box in Fig. 3).

The cell components in the enlarged box in Fig. 3 highlight the working principle of a BPM assembly where water is dissociated at the interface of a cationic (CEM) and an anionic (AEM) exchange membrane, before H<sup>+</sup> and OH<sup>-</sup> move in opposite directions. Unlike for AEM design, in the BPM design,

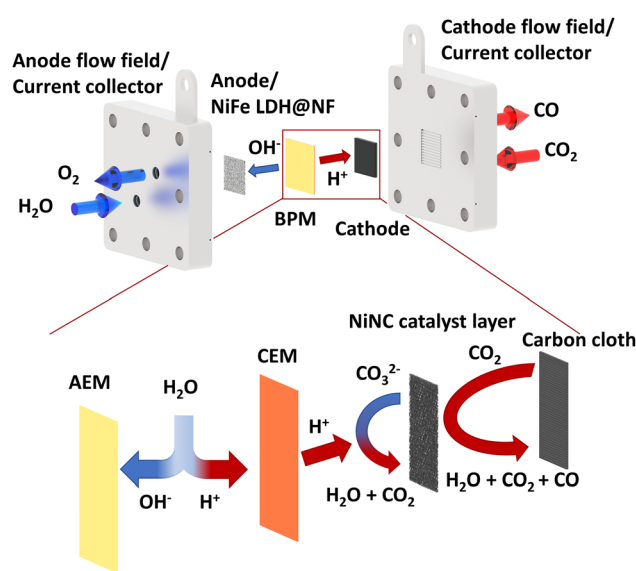
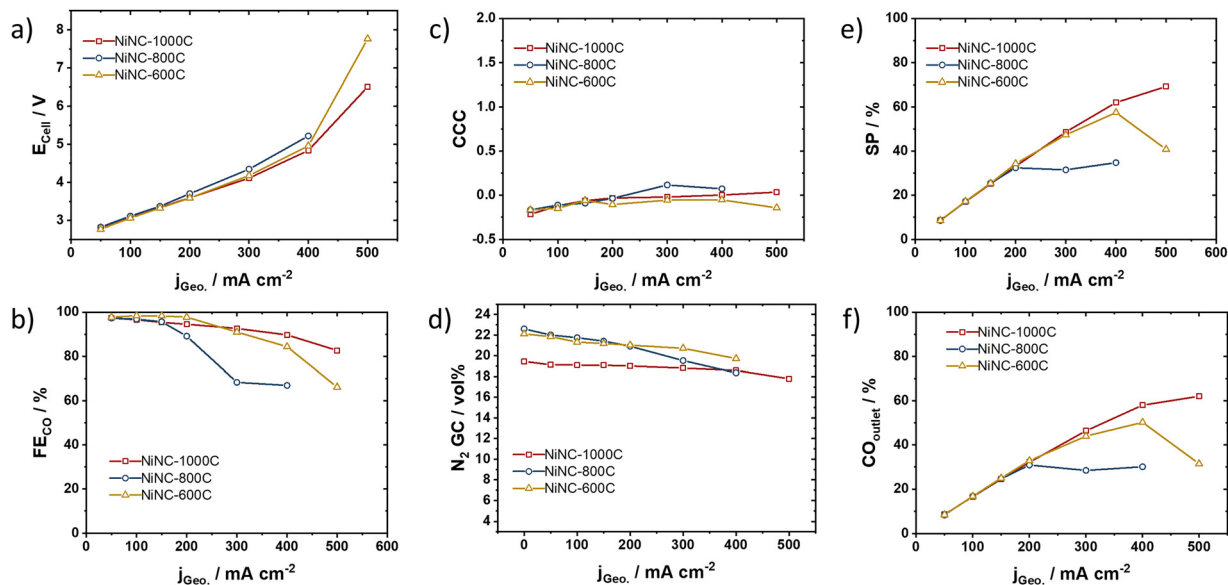


Fig. 2 Schematic of the zero gap ccs cell with insight in the BPM and cathode processes. The cell contains a flow field integrated current collector, a NiFe-LDH@NF anode, a bipolar membrane and a NiNC catalyst coated GDL. The insight shows the direction of the membrane, CEM to cathode, and the assumed neutralization of the carbonate by protons to recover CO<sub>2</sub>.





**Fig. 3** Electrochemical zero-gap cell performance. (a) Polarization curves of catalyst with different pyrolysis temperatures and (b) FE at different current densities. (c) The CCC proves that no carbonate formation is noticeable and (d)  $N_2$  vol% of the GC over different current densities to prove no flow depletion, expected 20 vol% ( $5 \text{ ml min}^{-1} N_2$  and  $20 \text{ ml min}^{-1} CO_2$ ). (e) Single pass conversion and  $CO_2$  to CO ratio at different current densities and (f) the CO ratio in the outlet stream of the electrolyzer cell. All test represent the mean value of at least 2 individual tests, the standard deviation can be found in the ESI.†

$OH^-$  move exclusively across the AEM to the anode. There, they help maintain the pH enabling the use of platinum-group-metal (PGM)-free anodes such as NiFe-LDH grown on nickel foam working as anode.<sup>42–44</sup> On the other hand, the protons move across the CEM to the cell cathode and buffer  $OH^-$  or  $CO_3^{2-}$  to water and  $CO_2$ , respectively. The  $OH^-$  are generated from the catalytic conversion of water to hydrogen or the conversion of  $CO_2$  to CO and form  $CO_3^{2-}$ . The  $H^+$  at the cathode will thus regenerate  $CO_2$ . For AEM electrolysis, techno-economic analysis showed that the  $CO_2$  membrane crossover in AEM systems coupled to subsequent anodic  $CO_2$  separation and regeneration is quite energy- and cost intensive.<sup>29,45</sup>

Fig. 3 shows six key cell performance parameters vs. the applied current density of the reverse-bias zero gap BPM electrolyzer cell, in particular cell voltage, CO faradaic efficiency ( $FE_{CO}$ ), carbon cross over coefficient (CCC),  $N_2$  vol% in cell outlet flow rate, single pass conversion (SP), and the CO concentration in the outlet flow. Each performance parameter was evaluated for each of the three NiNC cathode catalysts at a  $CO_2$  inlet flow rate of  $20 \text{ ml min}^{-1}$  or  $4 \text{ ml min}^{-1} \text{ cm}^{-2}$  in a current density range from 0–500  $\text{mA cm}^{-2}$ . The polarization curves (Fig. 3a) of all three cathodes were very similar up to 200  $\text{mA cm}^{-2}$ . Beyond that, the rise in cell voltage varied for each catalyst, likely as a result of increasing  $H_2$  faradaic efficiency ( $FE_{H_2}$ ) for the NiNC-600C and the NiNC-1000C. Drawing 500  $\text{mA cm}^{-2}$  proved problematic for NiNC-800C likely due to slow water dissociation rates. While trends in  $FE_{CO}$  (Fig. 3b) did not correlate with the pyrolysis temperatures, they followed trends in BET surface areas, suggesting a relation to catalyst porosity. Notably, despite the reverse-bias low-pH conditions at the cathode, the BPM cell reached

favorable  $FE_{CO}$  values of 80–100% at current densities up to 500  $\text{mA cm}^{-2}$ .

In order to characterize the ion transport in the cathodes of  $CO_2$  electrolyzers, we recently introduced the concept of the carbon cross over coefficient, CCC.<sup>16</sup> Illustrated in the context of a AEM  $CO_2$  electrolyzer,<sup>16</sup> the CCC proved a diagnostic tool to distinguish ion transport regimes dominated by protons (CCC  $\sim 0$ ), carbonate (CCC  $\sim 1$ ), or bicarbonate ions (CCC  $\sim 2$ ). Equivalently, the CCC provided insight in the non-electrocatalytic consumption of  $CO_2$  by  $OH^-$ .<sup>16</sup> Fig. 3c reports experimental CCC values in the present BPM  $CO_2$  electrolyzer environment. Unlike for AEM  $CO_2$  electrolyzers, the experimental CCC values are near 0 over the entire current density range, suggesting protons to be the dominant ion at the cathode and implying no significant loss of  $CO_2$  by carbonate formation. This directly confirms the hypothesized functional concept of a reverse-bias BPM-based cell cathode. Here, we further introduce the experimental volume fraction of  $N_2$  in the cell outlet (Fig. 3d) as a new diagnostic tool to characterize failure modes and degradation regimes of  $CO_2$  electrolyzers. A small  $N_2$  “bleed” is introduced after the cell and prior to the gas chromatographic analysis to provide an internal calibration for accurate determination of the outlet flow. For a  $CO_2$  to CO electrolyzer operating at  $FE_{CO} \sim 100\%$  without any non-electrocatalytic loss of  $CO_2$ , a constant  $N_2$  bleed of  $5 \text{ ml min}^{-1}$  against the  $CO_2$  inlet feed of  $20 \text{ ml min}^{-1}$  should result in an experimental  $N_2$  fraction of about 20 vol%, as evidenced in Fig. 3d. By contrast, in case of (b) carbonate formation from  $OH^-$  and  $CO_2$ , the volumetric outlet flow rate decreases, while the experimental  $N_2$  vol% increases. In absence of carbonate formation, yet significant competitive  $H_2$  evolution, the outlet



flow rate increases, while the  $N_2$  vol% decreases, as observed for NiNC-800C (blue line in Fig. 3d) above  $200 \text{ mA cm}^{-2}$  where the  $FE_{CO}$  gradually dropped. These considerations underline the diagnostic value of the  $N_2$  vol%, which will be elaborated further below. Next, the single pass conversions of the BPM electrolyzer were evaluated for each NiNC catalyst (Fig. 3e). Thanks to the low carbonate formation in the proton-rich cathode suggested by  $CCC \sim 0$ , the present BPM  $CO_2$  electrolyzer design displayed a very high  $\sim 70\%$  single pass conversion (SP) that significantly surpassed the theoretical limit of 50% of AEM  $CO_2$  electrolyzer systems that are characterized by  $CCC \sim 1$ . These favorable SP values resulted in CO-enriched outlet flows of up to 60 vol% at  $400\text{--}500 \text{ mA cm}^{-2}$  for NiNC-1000C (Fig. 3f) that are relevant for cascaded  $CO_2$  conversion using tandem electrolyzer cell designs<sup>46</sup> or other subsequent CO-based, e.g. synthesis gas related, thermal catalytic processes.

One of the challenges of BPM cell designs remained the limiting water dissociation rates at higher current densities coupled with high overpotentials. The Boettcher group showed how self-made BPMs overcome this challenge; we prepared CEM-AEM combinations<sup>47–49</sup> and succeeded in significantly decreasing cell potentials to below 4 V even at high current densities of  $600 \text{ mA cm}^{-2}$  (Fig. S9, ESI<sup>†</sup>). The significantly lowered cell voltage penalty using  $TiO_x$  water dissociation catalysts is testament to the technological viability of reversed-bias BPM electrolyzer schemes. It voids the commonly held view that excessive cell voltages will preclude the wider use of reverse-bias BPM cells. In Table S4 (ESI<sup>†</sup>) we can show that we could improve the achievable current density, faradaic efficiency and even lower drastically the cell potential.

We note that minor, though finite,  $K^+$  migration from anode to cathode across the BPM does impact the electroneutrality balance, as well.  $K^+$  transport rates lower the required water dissociation rate ( $H_2O \rightarrow H^+ + OH^-$ ) in the BPM. While this may benefit overpotentials, the resulting potassium carbonate formation may affect stability (Fig. S8a, ESI<sup>†</sup>) and promotes  $CO_2$  consumption. To lower  $K^+$  cross-over-rates, we carried out control experiments using 0.1 M KOH instead of 1 M KOH, which lowered the  $FE_{CO}$  (Fig. S8b, ESI<sup>†</sup>). There appears to exist a trade-off between product selectivity and  $K^+$  cross-over in BPM systems, in line with a previous report on Ag catalysts.<sup>30</sup>

## Failure mode diagnosis and stabilization of zero-gap BPM $CO_2$ electrolyzers

In order to learn more about the nature, the diagnosis, and the mitigation of failure modes of zero-gap BPM  $CO_2$  electrolyzers, we investigated the stability of the BPM cell at an initial constant current density of  $100 \text{ mA cm}^{-2}$  for 100 h. Fig. 4a and b report the temporal evolution of the cell voltage  $E_{cell}$ ,  $FE_{CO}$ ,  $FE_{H_2}$ , and  $N_2$  vol% over the test time. We observed an initial stable performance ( $FE_{CO} = 100\%$ ,  $N_2$  bleed = 20 vol%) below 3.25 V cell potential for around 10 h. This stable regime was followed by an unstable regime, characterized by increased,

fluctuating  $E_{cell}$  and scattered  $FE_{CO}$  and  $FE_{H_2}$ . During the unstable regime, the  $N_2$  vol% values rose to 100% (yellow period in Fig. 4b), followed by a period of fluctuating  $N_2$  vol% values (grey period in Fig. 4b). Correlating the dynamic performance parameters in Fig. 4a and b with an inspection of the cathodic  $CO_2$  gas channels, we realized that the  $N_2$  bleed vol% values provided a surprisingly useful diagnostic test for the detailed salt blocking locations (Fig. 4b and c):  $N_2$  vol% values of 100% correlated with complete salt blocking near the cell outlet (marked “outlet” in Fig. 4b). This is because during this particular type of salt blocking failure, the cell outlet gas flow ceased completely, while the  $N_2$  bleed flow rose to 100 vol%, being the only gas detected. Regimes with strongly fluctuating values of  $N_2$  vol%, by contrast, represented a failure mode characterized by dynamic partial salt blocking (marked “partial” in Fig. 4b). Incomplete dynamic salt blocks in the cathode flow channel led to reduced  $CO_2$  feeds. This causes the  $FE_{H_2}$  to rise in order to satisfy the applied current density. As a result of this,  $FE_{CO}$  and  $FE_{H_2}$  fluctuated irregularly. Occasional cathode flushing helped normalize the  $N_2$  vol% values, suggesting the removal of salt blocks.

We then tested the system stability at a constant current density of  $200 \text{ mA cm}^{-2}$  (Fig. 4d and e). After an initial stable regime at 3.7 V and  $FE_{CO} > 90\%$ , the cell entered its first failure mode regime after ca. 18 h. This failure regime appeared distinct from the one observed in Fig. 5a and b: while  $E_{cell}$  rose, and  $FE_{CO}$  dropped,  $N_2$  vol% and  $FE_{H_2}$  values stabilized at 40% and 20%, respectively, without fluctuations (yellow period in Fig. 5e). This failure regime involves salt blocking near the cell inlet (marked “inlet”), the location of which we were able to confirm experimentally (Fig. 4f). Inlet salt blocking is characterized by time-stable faradaic  $H_2$  evolution from water coupled to exclusive detection of  $H_2$  and  $N_2$  in the outlet flow, because  $CO_2$  input feed is blocked. Again, cathode flushing was able to alter or partially mitigate salt blocking (see  $> 65$  h), corroborating the importance of cathodic water management in zero-gap  $CO_2$  electrolyzers. Our stability studies hence suggested that our BPM zero-gap  $CO_2$  electrolyzer performance was limited by the system stability and not by any single component stability.

In AEM  $CO_2$  electrolyzer systems, salt block degradation can be addressed by (i) water management (ii) cell temperature adjustments or (iii) salt solubility increases, e.g., replacing  $K^+$  with  $Cs^+$ . We investigated whether these mitigation strategies would also apply to BPM  $CO_2$  electrolyzer and opted for strategy (iii). In a control experiment, we used a 200 ml 1 M CsOH anolyte at  $100 \text{ mA cm}^{-2}$ .

Use of Cs at the anode clearly solved failure modes associated with salt precipitation and allowed stable operation over at least 100 h at close to 100% FE, 3.25 V (Fig. 5a) and only a small pH change (from pH 14 to pH 13 after 100 h) at the anode. In order to verify that  $N_2$  vol% continues to act as diagnostic tool, we monitored  $N_2$  vol% values and confirmed their time-dependent stability at nearly 20% over 100 h. These results corroborate that the favorable solubility of Cs-(bi)-carbonate suppressed undesired salt blocking (Fig. 5b). We note in passing that, in our view, cell stability tests at



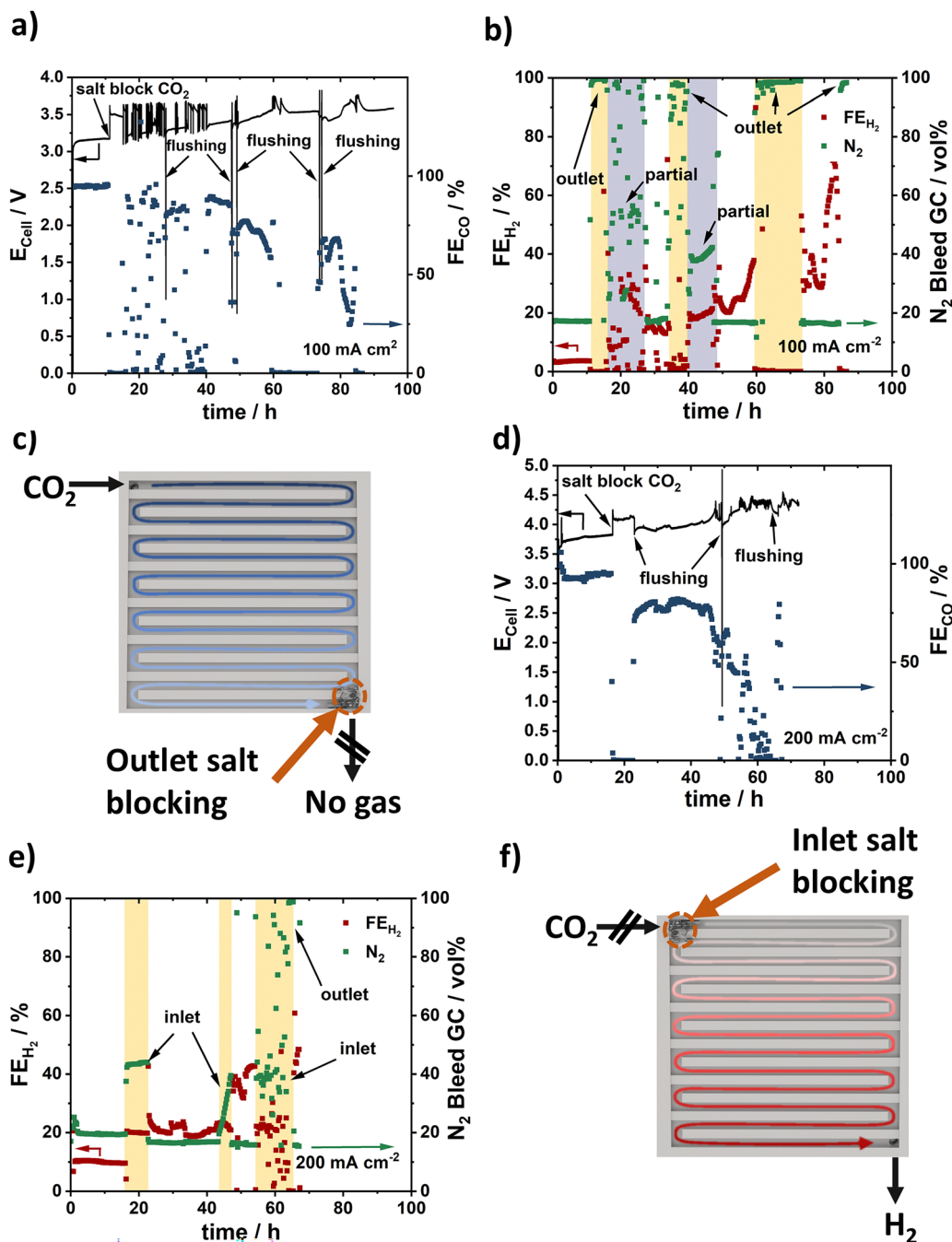


**Fig. 4** Electrochemical zero gap cell stability. (a) Cell voltage (solid line) and  $FE_{CO}$  (blue squares) during a 100 h stability test at constant current density of  $100 \text{ mA cm}^{-2}$ . Salt blocking failure events ("salt block  $CO_2$ ") are indicated. "flushing" marks salt removal by water flushing of cathode channel. (b)  $FE_{H_2}$  and actual  $N_2$  vol% in the exit flow. Expected  $N_2$  vol% from  $N_2$ -bleed is 20%. The  $N_2$  vol% is used as diagnostic tool to determine where and what type of cell blocking occurs. "outlet" (yellow periods) marks full-blocking failure regimes characterized by  $N_2$  vol%  $\sim 100\%$  coupled to  $FE_{H_2} \sim 0\%$  associated with complete flow blockage near cell outlet. "partial" (grey periods) marks partial blocking failure regimes characterized by very scattered  $N_2$  vol% values between 20% and 100%. (c) Schematic illustration of salt blocking at the cell exit derived from data in (b). (d) Cell voltage (solid line) and  $FE_{CO}$  (blue squares) during a 100 h stability test at constant current density of  $200 \text{ mA cm}^{-2}$ . (e)  $FE_{H_2}$  and actual  $N_2$  vol% in the exit flow. "inlet" (yellow periods) marks failure regimes characterized by elevated  $N_2$  vol%  $> 20\%$  and elevated  $FE_{H_2}$  associated with salt blockage near cell inlet. (f) Schematic illustration of salt blocking at the inlet of cell derived from data in (e).  $N_2$  bleed: 5 sccm,  $CO_2$  feed: 20 sccm. The data shown in the figure correspond to single tests.

current densities of about  $100 \text{ mA cm}^{-2}$  reveal system stability rather than catalyst component stability. This makes component stability tests in a liquid electrolyte environment of a commonly employed H-cell operating at even smaller current densities very doubtful. This is why we investigated the BPM

electrolyzer stability at higher current densities of  $200 \text{ mA cm}^{-2}$  at extended test times (Fig. S10, ESI†). For the initial 24 h, the cell performance maintained favorable 90%  $FE_{CO}$  with a slight rise in  $E_{cell}$  from 3.9 to 4.3 V. Then, we noticed a pH change on the anode to pH 8–9 after 140 h (100 h at  $100 \text{ mA cm}^{-2}$  and 40 h



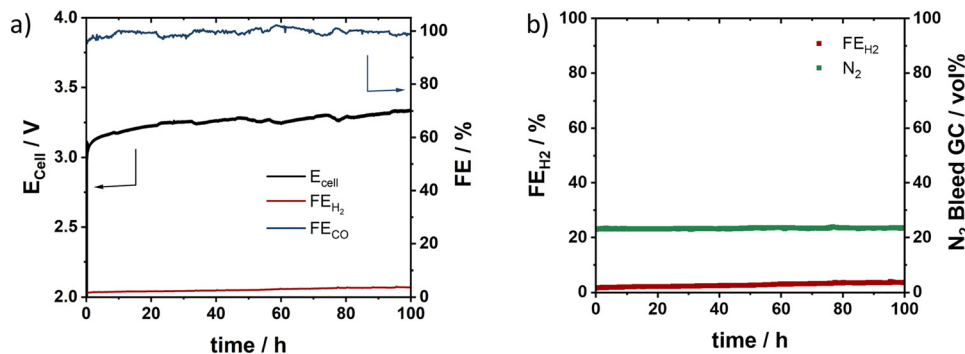


Fig. 5 Optimized stability test. (a) Cell voltage and FE of a stability test at  $100 \text{ mA cm}^{-2}$  using a  $1 \text{ M CsOH}$ . (b)  $\text{FE}_{\text{H}_2}$  and  $\text{N}_2$  vol% in the GC to prove no salt blocking. The data shown in the figure correspond to single tests.

at  $200 \text{ mA cm}^{-2}$ ). This was associated with a drastic black anolyte color suggesting corrosion of the Ni-based anode catalyst. Post-testing analysis of the anode revealed a clear morphology change at the front side of the anode (Fig. S11, ESI<sup>†</sup>) and we saw individual particles in the completely blackened anode (Fig. S12, ESI<sup>†</sup>) with the anode back side still resembling metallic Ni foam (Fig. S13, ESI<sup>†</sup>). Finally, after a test time of 170 h, the zero gap  $\text{CO}_2$  electrolyzer ceased operation with complete loss of CO selectivity. After disassembly, pinholes were observed all over the membrane, indicating possible impact of the anode restructuring. Clearly, when PGM-free anodes are used, tracking the evolution of anodic pH is critical.

## Conclusion

We have presented the first zero-gap reverse-bias BPM  $\text{CO}_2$ -to-CO electrolyzer cell deploying CO-selective single Ni atom cathode catalysts. Furthermore, we have reported the usefulness of the novel concept of the carbon crossover coefficient, CCC, and the  $\text{N}_2$  bleed as diagnostic tools to predict and understand the dominant transport ion and the type of failure regimes. We have analyzed key cell performance parameters and diagnosed its cell stability over 100+ hours. While use of a  $\text{N}_2$  bleed for internal reference has been known to be critical for accurate evaluation of cell performance, we now propose the experimental  $\text{N}_2$  vol% in the combined cell outlet and bleed flow to be a valuable diagnostic tool to recognize and analyze cell failure regimes due to cathodic salt blocking.

The zero-gap BPM  $\text{CO}_2$ -to-CO electrolyzer cell showed excellent performance over a wide current density range of 0 to  $500 \text{ mA cm}^{-2}$  with  $\text{FE}_{\text{CO}}$  near 100%. The proton-controlled ion transport in the cathode was confirmed by a carbon cross-over coefficient (CCC) near zero, suggesting minimal carbon loss due to carbonate formation. This was coupled with a high single pass conversion of  $\sim 70\%$  at the largest current densities.

The experimental  $\text{N}_2$  vol% values proved a diagnostic tool for the localization of system instabilities due to salt blocking. Complete salt blocking near the cell outlet resulted in experimental  $\text{N}_2$  volume fractions of close to 100%, as the gas outflow from the cell ceased. Salt blacks near the cell inlet resulted in time stable increases of the experimental  $\text{N}_2$  vol% to around

40%, with  $\text{FE}_{\text{H}_2}$  nearing 20%. Partial dynamic salt blocking, however, resulted in highly fluctuating values of  $\text{N}_2$ ,  $\text{FE}_{\text{CO}}$ , and  $\text{FE}_{\text{H}_2}$ .

Short term mitigation of system failure modes was achieved by cathodic water management. Increasing salt solubility, by contrast, proved a superior stabilization strategy for 100+ hours. Only at larger current densities (here  $200 \text{ mA cm}^{-2}$ ) and further extended test times (100–200 h), individual component stability failures became noticeable as anolytes approached near neutral pH. This should be considered when  $\text{CO}_2$  electrolysis component stability is evaluated in low-current and/or short-term H-Cell environments.

## Author contributions

Conceptualization: Sven Brückner and Ana Araújo. Investigation and formal analysis: Sven Brückner, Ana Araújo, Oleksandr Bondarchuk, Elvira Paz, Rosalia Cid, Isilda Amorim, Yu Zhipeng, Pierre Schröer, Florian Krebs, Philipp Hauke. Writing – original draft: Sven Brückner, Oleksandr Bondarchuk, Wen Ju. Writing – review & editing: all authors. Supervision: Peter Strasser, Oleksandr Bondarchuk, Manuel Fernando R. Pereira, Olívia Salomé G. P. Soares, Lifeng Liu. Funding acquisition: Peter Strasser, Oleksandr Bondarchuk, Manuel Fernando R. Pereira, Olívia Salomé G. P. Soares, Lifeng Liu, Ana Araújo.

## Data availability

The data supporting this article have been included as part of the ESI<sup>†</sup>.

## Conflicts of interest

The authors declare no competing interest.

## Acknowledgements

Funding: Technical University Berlin. The research leading to these results has received funding from the European Union's Horizon 2020 research and innovation programme under grant



agreement no. 851441, SELECTCO2. This work partially supported by national funds through FCT/MCTES (PIDDAC): LSRE-LCM, UIDB/50020/2020 (DOI: <https://doi.org/10.54499/UIDB/50020/2020>) and UIDP/50020/2020 (DOI: <https://doi.org/10.54499/UIDP/50020/2020>); and ALiCE, LA/P/0045/2020 (DOI: <https://doi.org/10.54499/LA/P/0045/2020>). Ana Araújo, acknowledges PhD Scholarship grant from FCT (SFRH/BD/143490/2019). OSGPS acknowledges FCT funding under the Scientific Employment Stimulus – Institutional Call CEECINST/00049/2018.

## References

- N. Hoshi, M. Kato and Y. Hori, Electrochemical reduction of CO on single crystal electrodes of silver Ag(111), Ag(100) and Ag(110), *J. Electroanal. Chem.*, 1997, **440**(1–2), 283–286.
- T. Hatsukade, K. P. Kuhl, E. R. Cave, D. N. Abram and T. F. Jaramillo, Insights into the electrocatalytic reduction of CO(2) on metallic silver surfaces, *Phys. Chem. Chem. Phys.*, 2014, **16**(27), 13814–13819.
- C. Kim, H. S. Jeon, T. Eom, M. S. Jee, H. Kim and C. M. Friend, *et al.*, Achieving Selective and Efficient Electrocatalytic Activity for CO<sub>2</sub> Reduction Using Immobilized Silver Nanoparticles, *J. Am. Chem. Soc.*, 2015, **137**(43), 13844–13850.
- S. Liu, H. Tao, L. Zeng, Q. Liu, Z. Xu and Q. Liu, *et al.*, Shape-Dependent Electrocatalytic Reduction of CO(2) to CO on Triangular Silver Nanoplates, *J. Am. Chem. Soc.*, 2017, **139**(6), 2160–2163.
- X. Yuan, Y. Wu, B. Jiang, Z. Wu, Z. Tao and X. Lu, *et al.*, Interface Engineering of Silver-Based Heterostructures for CO(2) Reduction Reaction, *ACS Appl. Mater. Interfaces*, 2020, **12**(50), 56642–56649.
- A. Ozden, Y. J. Liu, C. T. Dinh, J. Li, P. F. Ou and F. P. G. de Arquer, *et al.*, Gold Adparticles on Silver Combine Low Overpotential and High Selectivity in Electrochemical CO Conversion, *Acs Appl. Energy Mater.*, 2021, **4**(8), 7504–7512.
- A. S. Varela, N. Ranjbar Sahraie, J. Steinberg, W. Ju, H. S. Oh and P. Strasser, Metal-Doped Nitrogenated Carbon as an Efficient Catalyst for Direct CO<sub>2</sub> Electroreduction to CO and Hydrocarbons, *Angew. Chem.*, 2015, **127**(37), 10908–10912.
- W. Ju, A. Bagger, G. P. Hao, A. S. Varela, I. Sinev and V. Bon, *et al.*, Understanding activity and selectivity of metal-nitrogen-doped carbon catalysts for electrochemical reduction of CO(2), *Nat. Commun.*, 2017, **8**(1), 944.
- A. S. Varela, W. Ju, A. Bagger, P. Franco, J. Rossmeisl and P. Strasser, Electrochemical Reduction of CO on Metal-Nitrogen-Doped Carbon Catalysts, *ACS Catal.*, 2019, **9**(8), 7270–7284.
- C. Li, W. Ju, S. Vijay, J. Timoshenko, K. Mou and D. A. Cullen, *et al.*, Covalent Organic Framework (COF) Derived Ni-N-C Catalysts for Electrochemical CO(2) Reduction: Unraveling Fundamental Kinetic and Structural Parameters of the Active Sites, *Angew. Chem., Int. Ed.*, 2022, **61**(15), e202114707.
- H. Y. Jeong, M. Balamurugan, V. S. K. Choutipalli, E. S. Jeong, V. Subramanian and U. Sim, *et al.*, Achieving highly efficient CO to CO electroreduction exceeding 300 mA cm with single-atom nickel electrocatalysts, *J. Mater. Chem. A*, 2019, **7**(17), 10651–10661.
- T. T. Zheng, K. Jiang, N. Ta, Y. F. Hu, J. Zeng and J. Y. Liu, *et al.*, Large-Scale and Highly Selective CO Electrocatalytic Reduction on Nickel Single-Atom Catalyst, *Joule*, 2019, **3**(1), 265–278.
- S. J. Raaijman, N. Arulmozhi and M. T. M. Koper, Anisotropic Cathodic Corrosion of Gold Electrodes in the Absence and Presence of Carbon Monoxide, *J. Phys. Chem. C*, 2020, **124**(52), 28539–28554.
- T. J. P. Hersbach and M. T. M. Koper, Cathodic corrosion: 21st century insights into a 19th century phenomenon, *Curr. Opinion Electrochem.*, 2021, **26**.
- P. Prslja and N. López, Stability and Redispersion of Ni Nanoparticles Supported on N-Doped Carbons for the CO<sub>2</sub> Electrochemical Reduction, *ACS Catal.*, 2020, **11**(1), 88–94.
- S. Brückner, Q. Feng, W. Ju, D. Galliani, A. Testolin and M. Klingenhof, *et al.*, Design and diagnosis of high-performance CO<sub>2</sub>-to-CO electrolyzer cells, *Nat. Chem. Eng.*, 2024, **1**(3), 229–239.
- E. R. Cofell, U. O. Nwabara, S. S. Bhargava, D. E. Henckel and P. J. A. Kenis, Investigation of Electrolyte-Dependent Carbonate Formation on Gas Diffusion Electrodes for CO(2) Electrolysis, *ACS Appl. Mater. Interfaces*, 2021, **13**(13), 15132–15142.
- Y. Y. Gu, J. C. Wei, J. D. Li, L. Y. Wang and X. Wu, Long-term-stability continuous flow CO reduction electrolyzers with high current efficiency, *Sustainable Energy Fuels*, 2021, **5**(3), 758–766.
- W. Ren, X. Tan, C. Jia, A. Krammer, Q. Sun and J. Qu, *et al.*, Electronic Regulation of Nickel Single Atoms by Confined Nickel Nanoparticles for Energy-Efficient CO(2) Electroreduction, *Angew. Chem., Int. Ed.*, 2022, **61**(26), e202203335.
- G. O. Larrazabal, P. Strom-Hansen, J. P. Heli, K. Zeiter, K. T. Therkildsen and I. Chorkendorff, *et al.*, Analysis of Mass Flows and Membrane Cross-over in CO(2) Reduction at High Current Densities in an MEA-Type Electrolyzer, *ACS Appl. Mater. Interfaces*, 2019, **11**(44), 41281–41288.
- G. O. Larrazabal, M. Ma and B. Seger, A Comprehensive Approach to Investigate CO<sub>2</sub> Reduction Electrocatalysts at High Current Densities, *Acc. Mater. Res.*, 2021, **2**(4), 220–229.
- H. Yang, Q. Lin, C. Zhang, X. Yu, Z. Cheng and G. Li, *et al.*, Carbon dioxide electroreduction on single-atom nickel decorated carbon membranes with industry compatible current densities, *Nat. Commun.*, 2020, **11**(1), 593.
- X. Lv, Q. Liu, H. Yang, J. Wang, X. Wu and X. Li, *et al.*, Nanoconfined Molecular Catalysts in Integrated Gas Diffusion Electrodes for High-Current-Density CO<sub>2</sub> Electroreduction, *Adv. Funct. Mater.*, 2023, **33**(32), 2301334.
- A. Vass, B. Endrodi, G. F. Samu, A. Balog, A. Kormanyos and S. Cherevko, *et al.*, Local Chemical Environment Governs Anode Processes in CO(2) Electrolyzers, *ACS Energy Lett.*, 2021, **6**(11), 3801–3808.
- A. Vass, A. Kormanyos, Z. Koszo, B. Endrodi and C. Janaky, Anode Catalysts in CO(2) Electrolysis: Challenges and



- Untapped Opportunities, *ACS Catal.*, 2022, **12**(2), 1037–1051.
- 26 D. A. Vermaas and W. A. Smith, Synergistic Electrochemical CO Reduction and Water Oxidation with a Bipolar Membrane, *ACS Energy Lett.*, 2016, **1**(6), 1143–1148.
- 27 D. M. Weekes, D. A. Salvatore, A. Reyes, A. Huang and C. P. Berlinguette, Electrolytic CO(2) Reduction in a Flow Cell, *Acc. Chem. Res.*, 2018, **51**(4), 910–918.
- 28 M. A. Blommaert, D. Aili, R. A. Tufa, Q. Li, W. A. Smith and D. A. Vermaas, Insights and Challenges for Applying Bipolar Membranes in Advanced Electrochemical Energy Systems, *ACS Energy Lett.*, 2021, **6**(7), 2539–2548.
- 29 M. A. Blommaert, S. Subramanian, K. Yang, W. A. Smith and D. A. Vermaas, High Indirect Energy Consumption in AEM-Based CO(2) Electrolyzers Demonstrates the Potential of Bipolar Membranes, *ACS Appl. Mater. Interfaces*, 2022, **14**(1), 557–563.
- 30 K. Yang, M. Li, S. Subramanian, M. A. Blommaert, W. A. Smith and T. Burdyny, Cation-Driven Increases of CO(2) Utilization in a Bipolar Membrane Electrode Assembly for CO(2) Electrolysis, *ACS Energy Lett.*, 2021, **6**(12), 4291–4298.
- 31 K. Xie, R. K. Miao, A. Ozden, S. Liu, Z. Chen and C. T. Dinh, *et al.*, Bipolar membrane electrolyzers enable high single-pass CO(2) electroreduction to multicarbon products, *Nat. Commun.*, 2022, **13**(1), 3609.
- 32 A. Bagger, W. Ju, A. S. Varela, P. Strasser and J. Rossmeisl, Single site porphyrine-like structures advantages over metals for selective electrochemical CO reduction, *Catal. Today*, 2017, **288**, 74–78.
- 33 S. Vijay, W. Ju, S. Bruckner, S. C. Tsang, P. Strasser and K. R. Chan, Unified mechanistic understanding of CO reduction to CO on transition metal and single atom catalysts, *Nat. Catal.*, 2021, **4**(12), 1024–1031.
- 34 P. S. Bagus, C. J. Nelin, C. R. Brundle, B. V. Crist, E. S. Ilton and N. Lahiri, *et al.*, Main and Satellite Features in the Ni 2p XPS of NiO, *Inorg. Chem.*, 2022, **61**(45), 18077–18094.
- 35 A. P. Grosvenor, B. A. Kobe, M. C. Biesinger and N. S. McIntyre, Investigation of multiplet splitting of Fe 2p XPS spectra and bonding in iron compounds, *Surf. Interface Anal.*, 2004, **36**(12), 1564–1574.
- 36 M. C. Biesinger, L. W. Lau, A. R. Gerson and R. S. Smart, The role of the Auger parameter in XPS studies of nickel metal, halides and oxides, *Phys. Chem. Chem. Phys.*, 2012, **14**(7), 2434–2442.
- 37 G. I. Svirskiy, N. N. Sergeeva, S. A. Krasnikov, N. A. Vinogradov, Y. N. Sergeeva and A. A. Cafolla, *et al.*, Electronic structure of nickel porphyrin NiP: Study by X-ray photoelectron and absorption spectroscopy, *Phys. Solid State*, 2017, **59**(2), 368–377.
- 38 J. Li, S. Y. Hu, Y. Li, X. B. Fan, F. B. Zhang and G. L. Zhang, *et al.*, Pyrrolic N anchored atomic Ni-N<sub>3</sub>-C catalyst for highly effective electroreduction of CO<sub>2</sub> into CO, *Carbon*, 2023, **206**, 62–71.
- 39 P. Hou, X. Wang, Z. Wang and P. Kang, Gas Phase Electrolysis of Carbon Dioxide to Carbon Monoxide Using Nickel Nitride as the Carbon Enrichment Catalyst, *ACS Appl. Mater. Interfaces*, 2018, **10**(44), 38024–38031.
- 40 O. Bondarchuk, A. Morel, D. Bélanger, E. Goikolea, T. Brousse and R. Mysyk, Thin films of pure vanadium nitride: Evidence for anomalous non-faradaic capacitance, *J. Power Sources*, 2016, **324**, 439–446.
- 41 M. T. Nichols, W. Li, D. Pei, G. A. Antonelli, Q. Lin and S. Banna, *et al.*, Measurement of bandgap energies in low-k organosilicates, *J. Appl. Phys.*, 2014, **115**(9), 094105.
- 42 P. Hauke, M. Klingenhof, X. L. Wang, J. F. de Arau and P. Strasser, Article Efficient electrolysis of 5-hydroxymethylfurfural to the biopolymer-precursor furandicarboxylic acid in a zero-gap MEA-type electrolyzer, *Cell Rep. Phys. Sci.*, 2021, **2**(12), 100650.
- 43 P. Hauke, S. Brückner and P. Strasser, Paired Electrocatalytic Valorization of CO and Hydroxymethylfurfural in a Noble Metal-free Bipolar Membrane Electrolyzer, *ACS Sustainable Chem. Eng.*, 2023, **11**(37), 13628–13635.
- 44 M. Klingenhof, P. Hauke, M. Kroschel, X. L. Wang, T. Merzdorf and C. Binninger, *et al.*, Anion-Tuned Layered Double Hydroxide Anodes for Anion Exchange Membrane Water Electrolyzers: From Catalyst Screening to Single-Cell Performance, *ACS Energy Lett.*, 2022, **7**(10), 3415–3422.
- 45 T. Alerte, J. P. Edwards, C. M. Gabardo, C. P. O'Brien, A. Gaona and J. Wicks, *et al.*, Downstream of the CO<sub>2</sub> Electrolyzer: Assessing the Energy Intensity of Product Separation, *ACS Energy Lett.*, 2021, **6**(12), 4405–4412.
- 46 T. Moller, M. Filippi, S. Bruckner, W. Ju and P. A. Strasser, CO(2) electrolyzer tandem cell system for CO(2)-CO co-feed valorization in a Ni-N-C/Cu-catalyzed reaction cascade, *Nat. Commun.*, 2023, **14**(1), 5680.
- 47 Y.-L. Kao, L. Chen, S. W. Boettcher and D. Aili, Divergent Synthesis of Bipolar Membranes Combining Strong Interfacial Adhesion and High-Rate Capability, *ACS Energy Lett.*, 2024, **9**(6), 2953–2959.
- 48 L. Chen, Q. Xu, S. Z. Oener, K. Fabrizio and S. W. Boettcher, Design principles for water dissociation catalysts in high-performance bipolar membranes, *Nat. Commun.*, 2022, **13**(1), 3846.
- 49 J. C. Bui, E. W. Lees, D. H. Marin, T. N. Stovall, L. Chen and A. Kusoglu, *et al.*, Multi-scale physics of bipolar membranes in electrochemical processes, *Nat. Chem. Eng.*, 2024, **1**(1), 45–60.

